Climate Dynamics (2020) 55:1631–1647
https://doi.org/10.1007/s00382-020-05349-5

CO_2-induced heat source changes over the Tibetan Plateau in boreal summer-part II: the effects of CO_2 direct radiation and uniform sea surface warming

Xia Qu[1,2] · **Gang Huang**[2,3,4]

Received: 12 March 2020 / Accepted: 21 June 2020 / Published online: 29 June 2020

Abstract
Under the global warming, the influence of increased CO_2 on regional climate change is driven by two main effects: CO_2 direct radiation and oceanic warming. Based on the outputs of CMIP5 (phase 5 of the Coupled Model Intercomparison Project), the present study found that CO_2 direct radiation and uniform oceanic warming are mainly responsible for the heat source (HS) enhancement led by increased CO_2 during June–September over the Tibetan Plateau (TP). As CO_2 increases, the resulting uniform sea surface warming induces atmospheric warming and increased atmospheric moisture over the TP, which locally enhances the latent heating (LH). In addition, the uniform sea surface warming narrows the land-sea thermal contrast between the Asian continent and the Indo-Pacific and reduces the ascending motion of the air over the TP. This reduction of ascending motion is offsetted by the effect of CO_2 direct radiation, which enhances the thermal contrast and the ascending motion. The combined effect of the two causes a generally mild change in ascending motion. Evaporation intensification led by uniform sea surface warming partly contributes to the LH increase. Thus, the changes in LH lead to the enhancement of the TP HS. Additionally, the net radiation of the atmosphere over the TP slightly increases and partly hinders the HS increase, which is mainly associated with the effect of uniform sea surface warming. The leading intermodel spread of the TP HS features an overall positive/negative deviation pattern relative to the multi-model ensemble (MME) mean response caused by the LH diversity, which stems from the uncertainties of uniform sea surface warming and the corresponding temperature response over the TP among the models.

Keywords The tibetan plateau · Heat source · CO_2 direct radiation · Uniform sea surface warming

1 Introduction

The Tibetan Plateau (TP) is a huge Eurasian plateau that is a large heat source (HS), and it makes nearby climate unique across Northern Hemisphere (Li and Yanai 1996). In boreal summer, the TP heating and insulating effect result in monsoon rainfall in South Asia (Boos and Kuang 2010; Wu et al. 2012; Song et al. 2010; He et al. 2019). The rainfall-associated latent heating (LH) together with the TP heating reinforce the Asia monsoon circulation, and this reinforcement makes Asia the most poleward monsoon domain on Earth (Liu et al. 2007; Lee et al. 2015; Wang and Ding 2008; He et al. 2019); in addition, the heating gives rise to southwesterly flow over the Arabian Sea and Indian Peninsula, supplying moisture to the South Asian monsoon region and acting to climatologically cool the Arabian Sea (Kitoh 2004). The warm atmosphere led by the heating of the TP and South Asian monsoon combines with the mid-troposphere

✉ Xia Qu
quxia@mail.iap.ac.cn

[1] Center for Monsoon System Research, Institute of Atmospheric Physics, Chinese Academy of Sciences, P. O. Box 9804, Beijing 100029, China

[2] State Key Laboratory of Numerical Modeling for Atmospheric Sciences and Geophysical Fluid Dynamics, Institute of Atmospheric Physics, Chinese Academy of Sciences, Beijing 100029, China

[3] Laboratory for Regional Oceanography and Numerical Modeling, Qingdao National Laboratory for Marine Science and Technology, Qingdao 266237, China

[4] University of Chinese Academy of Sciences, Beijing 100049, China

westerlies and induces warm horizontal temperature advection that penetrates into the northern Pacific region. This advection is an important forcing of the mei-yu/baiu rainbelt (Sampe and Xie 2010). Additionally, the TP HS modulates the seasonal change of the Asian monsoon (Yeh and Wu 1998). Simulations (Abe et al. 2013; Zhao et al. 2019) suggest that the existence of TP heating in May may result in a cooler Arabian Sea, stabilizing the above atmosphere and postponing the onset of the monsoon over the Arabian Sea and Indian region.

Since the Industrial Revolution, the CO_2 concentration in the atmosphere has been increasing. This increase has a profound influence on climate (Stocker et al. 2013), as well as the HS over the TP (Qu et al. 2020). The outputs of the CMIP5 (phase 5 of the Coupled Model Intercomparison Project; Taylor et al. 2012) models have revealed that when the effects of the other forcings (e.g., aerosols, natural forcings, etc.) were excluded, the increased CO_2 led to a rise in the HS over the TP during June–September (Qu et al. 2020). Under increased CO_2, over the TP, the enhancement of atmosphere moisture and evaporation increase the LH released to the atmosphere, which led to an intensified HS. Concurrently, the mild intensification of the net radiation out of the atmosphere, mainly led by atmospheric warming, slightly hindered the rise in the HS. In terms of the intermodel spread of the HS enhancement among the CMIP5 models, the spread of local LH is mainly responsible for it.

The effects of the increased CO_2 on the atmosphere can mainly be divided into two kinds of effects. One is the effect of CO_2 direct radiation. The increased CO_2 leads to an enhancement of downwards radiation. Excluding the response of the ocean, the radiation increase leads to a rise in land surface temperature and modulates the other climate variables (e.g., Kamae et al. 2015; Sherwood et al. 2015). The other effect is the sea surface temperature (SST)-mediated effect in which the increased CO_2 radiative forcing warms the ocean, thereby influencing the global climate via dynamic and thermodynamic processes (e.g., Bony et al. 2013; Ma et al. 2012; Shaw and Voigt 2015). The SST-mediated effect is further decomposed into effects of the uniform sea surface warming and SST pattern, which is the SST-mediated effect minus the effect of uniform sea surface warming (He and Soden 2015; Huang et al. 2013). The outputs of CMIP5 reveal that CO_2 direct radiation strengthens the land-sea thermal contrast (Kamae et al. 2014) and enhances the moisture convergence as well as the rainfall over the Asia monsoon domain (Li and Ting 2017). The uniform sea surface warming warms the ocean, which in turn heats the global atmosphere and moisturizes the atmosphere, and it also narrows the land-sea thermal contrast (Kamae et al. 2014), thereby resulting in mild moisture convergence and rainfall over the Asia monsoon region (Li and Ting 2017; Endo et al. 2018). The SST pattern change affects the rainfall. Under global warming, the rainfall tends to increase in areas with a stronger SST increase relative to tropical mean SST change (Xie et al. 2010). Over winter, the uniform SST rise warms the TP surface and enhances the sensible heating (Qu et al. 2019).

Although Qu et al. (2020) revealed the total effects of increased CO_2 on the HS change over the TP, the contributions of the processes mentioned in last paragraph are not clear. Meanwhile, in light of the distinct responses of Asia monsoon rainfall to the two kinds of CO_2 effects (Li and Ting 2017; Endo et al. 2018), the CO_2 direct radiation and SST-mediated effects on the TP HS is interesting study topics that can contribute to a better understanding of associated dynamics and thermodynamic processes.

To meet the above objectives, the rest of this paper is organized as follows. Section 2 introduces the data and methods. Section 3 presents the total effects of the increased CO_2 on the HS change over the TP. Section 4 investigates the effects of CO_2 direct radiation and uniform sea surface warming on the TP LH change. Section 5 studies the net radiation of the atmosphere in response to CO_2 direct radiation and uniform sea surface warming. Section 6 investigates the origins of the leading intermodel spread of the TP HS among the models. Section 7 provides a summary and discussion.

2 Data and methods

2.1 CMIP5 experiments

The present study is based on monthly outputs of CMIP5 models (Taylor et al. 2012). The 11 models chosen in this manuscript contain full experiments associated with the effects of CO_2 direct radiation and SST-mediated effects. Information on the models is listed in Table 1. Note that CanAM4 and HadGEM2-A are the corresponding atmospheric general circulation models of CanESM2 and HadGEM2-ES, respectively. The experiments are as follows: (1) 1% CO_2 experiment, in which the coupled general circulation models are forced by CO_2 increases of 1% per year until the CO_2 concentration is quadrupled; (2) amip experiment, in which the models are run with the observed SST, sea ice, anthropogenic and natural forcing from 1979 to 2008; (3) amip4K experiment, in which the parameters are the same as in the amip experiment except that the SST forcing is increased by 4 K; (4) amipFuture experiment, in which the parameters are the same as in the amip experiment except that the SST forcing is derived from the multimodel ensemble (MME) mean of the 1% to quadrupled CO_2 experiment of the Coupled Model Intercomparison Project phase 3 models; and (5) amip4xCO2 experiment, in which the parameters are the same as those in the amip experiment except that

Table 1 Information for the climate models (source https://cmip-pcmdi.llnl.gov/cmip5/docs/CMIP5_modeling_groups.pdf)

No	Model ID (No.)	Modeling center (or group)
1	BCC-CSM1.1	Beijing Climate Center, China Meteorological Administration
2	CanESM2/CanAM4	Canadian Centre for Climate Modelling and Analysis, Canada
3	CCSM4	National Center for Atmospheric Research, USA
4	CNRM-CM5	Centre National de Recherches Météorologiques, Centre Européen de Recherche et de Formation Avancée en Calcul Scientifique, France
5	HadGEM2-ES/HadGEM2-A	Met Office Hadley Centre, UK
6	IPSL-CM5A-LR	Institut Pierre Simon Laplace, France
7	IPSL-CM5B-LR	
8	MIROC5	Atmosphere and Ocean Research Institute (The University of Tokyo), National Institute for Environmental Studies, and Japan Agency for MIROC5 Marine-Earth Science and Technology, Japan
9	MPI-ESM-LR	Max Planck Institute for Meteorology
10	MPI-ESM-MR	
11	MRI-CGCM3	Meteorological Research Institute

the CO_2 concentration is quadrupled from the values from 1979–2008. Only the "r1i1p1" run of the CMIP5 results is analyzed. The snow cover data in CCSM4, HadGEM2-ES (HadGEM2-A), IPSL-CM5A-LR and IPSL-CM5B-LR are unavailable. Surface specific humidity data of bcc-csm1-1, MPI-ESM-LR and MPI-ESM-MR are not available.

2.2 Methods

The total response to CO_2 increase represents the difference between the climatology during years 121–140 and that during years 1–20 in the 1% CO_2 experiment. Because this response represents the results of coupled general circulation models, we name it "CGCM" for conciseness. The role of uniform (nonuniform) sea surface warming, denoted "USST" ("USST + PAT"), is represented by the difference between the amip4K (amipFuture) and amip experiments. The "USST + PAT" is used to detect the SST-mediated effect of CO_2. The direct radiative effect of CO_2 is represented by the difference between the amip4xCO2 and amip experiments. This radiative effect is named "CO_2" for convenience (note that it is different than "CO_2"). In experiments 2–5, the results from 1979–2008 are studied.

To fairly compare the experiment results, some results are scaled to the same global mean SST or CO_2 change. We named the global mean SST change in the CGCM, USST and USST + PAT results "SST_{CGCM}", "SST_{USST}" and "$SST_{USST+PAT}$", respectively. The SST_{CGCM}, SST_{USST} and $SST_{USST+PAT}$ values of the models are listed in Table 2. To understand the contribution of uniform sea surface warming to the "CGCM", the USST results in each model are multiplied by SST_{CGCM}/SST_{USST} in order to normalize the global SST changes of USST and CGCM to the same level. Similarly, the "USST + PAT" results in each model are multiplied by $SST_{CGCM}/SST_{USST+PAT}$. The scaled "USST + PAT" results minus the scaled "USST" results denotes the effect of "PAT". Following Endo et al. (2018), the CO_2 results are multiplied by ln(3.3)/ln(4) so that the CO_2-induced radiation change is the same as that of the "CGCM". The scaling is widely used in former studies (e.g., Endo et al. 2018; Huang et al. 2013; Kamae et al. 2016). In addition, the tropical mean SST (25°S–25°N) and the global mean surface temperature are applied to scale the results and it does not change the qualitative results.

Table 2 Global mean SST changes (unit: K)

Model ID	CGCM $SST_{121-140} - SST_{1-20}$	amip4K-amip	amipFuture-amip
bcc-csm1-1	3.16	4.07	4.14
CanESM2 (CanAM4)	3.79	3.97	4.09
CCSM4	2.98	4.08	4.17
CNRM-CM5	3.65	4.02	4.01
HadGEM2-ES (HadGEM2-A)	3.78	4.03	4.12
IPSL-CM5A-LR	3.65	4.06	3.90
IPSL-CM5B-LR	2.78	4.12	4.20
MIROC5	2.68	4.09	4.14
MPI-ESM-LR	3.35	3.95	4.08
MPI-ESM-MR	3.30	3.95	3.93
MRI-CGCM3	3.05	4.09	4.17

To study the responses of the CMIP5 models, the study uses the MME method. In addition, the 95% confidence intervals (CIs) among the models are provided to identify the significance of the signal. To facilitate the analysis of the MME and CIs, we used a bilinear interpolation technique to interpolate the data onto a $1.0° \times 1.0°$ grid. Note that the

interpolation was not performed when we computed the area average.

To study the intermodel spread, an intermodel empirical orthogonal function (EOF) method was employed. The intermodel EOF is widely used to detect model diversity (e.g., Li and Xie 2014; Ma and Xie 2013; Qu 2017). Traditionally, the EOF analysis is performed on 3-dimensional variables (one dimension is time). In the intermodel EOF analysis, we regard the spatial pattern of the 1st model as the result of "time step 1", the spatial pattern of 2nd model as "time step 2", and so on. The EOF results of this 3-dimensional variable are the spatial patterns of the intermodel spread around the MME mean result. For a given model, the corresponding principle component is the magnitude of the spread feature departed from the MME mean.

2.3 Calculation of the HS

Following previous studies (Duan and Wu 2008; Li and Yanai 1996; Luo and Yanai 1984), the HS of the atmosphere column is as follows:

$$\mathrm{HS} = LP + \mathrm{SH} + \mathrm{R_{net}} \quad (1)$$

where $L = 2{,}500{,}632\ \mathrm{J\ kg^{-1}}$; and P, SH, and $\mathrm{R_{net}}$ are the precipitation, the surface sensible heating and the net radiation flux into the atmospheric column, respectively.

The net radiation flux into the atmospheric column is as follows:

$$\mathrm{R_{net}} = L_s\uparrow - L_s\downarrow + S_s\uparrow - S_s\downarrow + S_t\downarrow - L_t\uparrow - S_t\uparrow \quad (2)$$

where L and S represent the longwave and shortwave radiation, respectively; the symbols ↑ and ↓ mean upwelling and downwelling radiation, respectively; and the subscripts "s" and "t" mean radiation flux at the surface and the top of the atmosphere (TOA), respectively.

3 Total effects of increased CO_2

Before the study, a verification was performed to determine whether the findings of the 11 chosen models are close to those of the 30 models adopted in Qu et al. (2020). The results are displayed in Appendix. For the response associated with the TP HS during June–September (JJAS), significant differences were not found between the results of the 11 models and 30 models. Thus, the 11-model results used in this study are capable of representing the 30-model results.

During JJAS, the TP is dominant by increased HS in the MME of the CGCM results (Fig. 1a). Significant increases are mainly observed over the southern and eastern TP. The CO_2 direct radiative effect contributes to a uniform enhancement of the HS over the TP (Fig. 1b). The uniform sea surface warming may lead to a nearly uniform but slightly weakening TP HS (Fig. 1c). The SST pattern contributes to a mild decrease in the HS over the southern TP (Fig. 1d). The combinations of the effects are displayed in Fig. 1e–h. Among the combinations, the spatial patterns of "CO2 + USST" and "CO2 + USST + PAT" are close to that of the JJAS HS over the TP (Fig. 1a, e, h). The spatial correlation coefficient of "CO2 + USST" HS with "CGCM" HS is 0.89, and the coefficient of "CO2 + USST + PAT" with "CGCM" HS is slightly lower at 0.81. The ratio of the spatial standardized deviation of "CO2 + USST" HS to that of "CGCM" HS is 0.91, and the corresponding ratio of "CO2 + USST + PAT" to "CGCM" is 0.63. The HS increase over the southern TP for "CO2 + USST + PAT" is less significant than that of "CO2 + USST". Thus, the response pattern of JJAS HS to increased CO_2 over the TP is largely

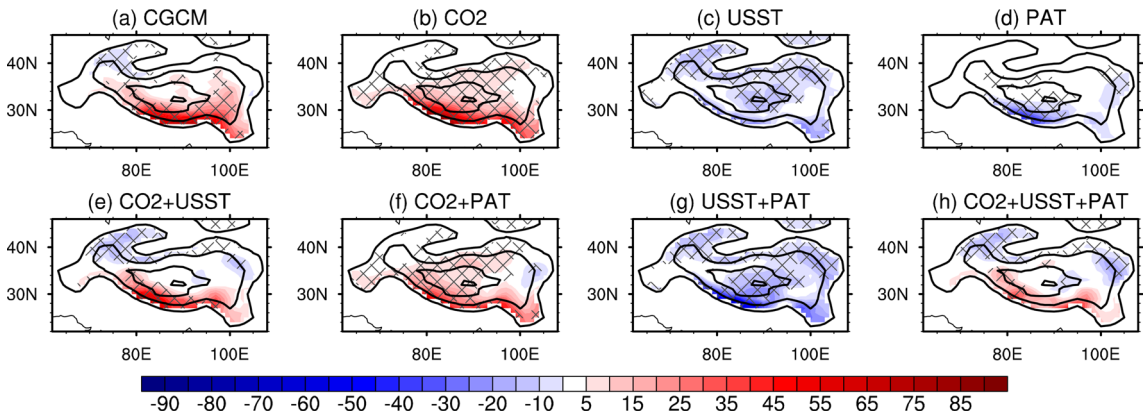

Fig. 1 Responses (color shading) of the JJAS HS. **a**–**h** Results of CGCM, CO2, USST, PAT, CO2+USST, CO2+PAT, USST+PAT and CO2+USST+PAT. Unit: W m^{-2}. The responses are the MME results. The contours represent the elevations of 1500 m, 3000 m, 5000 m and 6000 m; and the lattices indicate that the response reached the 95% significance level

determined by the combined effect of CO_2 direct radiation and uniform sea surface warming.

The TP-average response of the HS and the associated components is also largely explained by the sum of CO_2 and USST. For the HS and LH, CO_2 direct radiation is the main contributor (Fig. 2). For the CGCM results, the MME of the HS and LH increased by 12.6 and 14.6 W m^{-2} respectively, whereas for the CO2 results, these values are 12.1 and 10.5 W m^{-2}, respectively. The uniform sea surface warming mainly contributes to the change in the net radiation of the atmosphere (Fig. 2). The SST pattern prevents the HS and LH intensification over the TP and has a slight influence on the net radiation of the atmosphere. The sum of CO_2 and USST well reproduces the overall features of the responses associated with the HS over the TP, including the increase in the HS, LH and net radiation of the atmosphere (Fig. 2). However, the HS response of the sum of CO_2 and USST is less significant, which is because of the opposite-sign response in spatial pattern over the TP region (Fig. 1e). In addition, the general features of the TP-averaged radiation fluxes are well reproduced by the sum of CO_2 and USST. The features include the enhancement of all the longwave radiation at the TP surface and the TOA and the reduction of the upwelling shortwave at the surface and the TOA. The downwelling shortwave radiation is less significant than that in the CGCM results.

In addition, it is revealed in Sect. 6 that the model spread of the TP HS response is also largely explained by the sum of CO_2 and USST.

Therefore, in terms of the spatial pattern, area average and model spread, the JJAS HS response over the TP is able to be largely explained by the sum of CO_2 and USST. If only considering the TP-averaged change, most of the associated features (e.g., net radiation of the atmosphere and its components) is able to be reproduced by the sum of the CO_2 and USST. The following mainly emphasize the effects of the CO_2 and USST.

4 Latent heating

In terms of the spatial pattern of the HS response over the TP, the LH is the most important contributor in the CGCM, CO_2 and USST results. A Taylor diagram (Fig. 3) is provided to show the contributions of the components to the spatial pattern of the JJAS HS response over the TP. The ratio of the spatial standardized deviation and the spatial correlations are indicated by the radial distance and radial angle, respectively; and the distance to "REF" is the center root-mean-square error. The grid boxes at or above 1500 m are used to calculate the standardized deviation and correlation. In the CGCM, CO_2 and USST results, the LH is the closest to the "REF" among the components. The contributions of the surface sensible heating and net radiation of atmosphere are marginal.

To understand the LH change, the moisture budget analysis was employed. Based on Luo and Yanai (1984) and Chou et al. (2009), the LH (which equals to *LP*) change is written as follows:

$$LP' \approx \left\langle -L\overline{\mathbf{V}} \cdot \nabla q' \right\rangle + \left\langle -L\mathbf{V}' \cdot \nabla \overline{q} \right\rangle + \left\langle -L\overline{\omega}\partial_p q' \right\rangle + \left\langle -L\omega'\partial_p \overline{q} \right\rangle + LE \quad (3)$$

where $L = 2{,}500{,}632$ J kg^{-1}; $\mathbf{V}$, ω, q and E are the horizontal wind, pressure velocity, specific humidity and evaporation, respectively; an overbar and prime indicate the climatology and change, respectively; and angle brackets, <>, represent mass integration from the surface to 100 hPa.

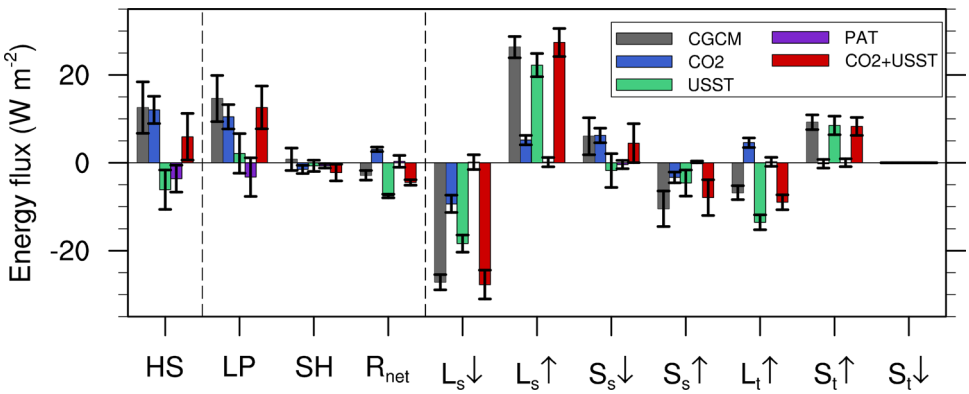

Fig. 2 JJAS-averaged responses of the HS and associated components, as well as the radiation fluxes at the surface and the TOA. The bars in gray, blue, green, purple and red are the MME results of CGCM, CO2, USST, PAT and CO2+USST, respectively. Only those grid boxes at or above 3000 m over the TP were used to compute the average. The downwelling longwave and shortwave radiations and the upwelling longwave and shortwave radiations are multiplied by − 1. Therefore, positive and negative values indicate contributions of heat gain and loss of the atmospheric column, respectively. Unit: W m^{-2}. The error bars represent the 95% CIs of the changes

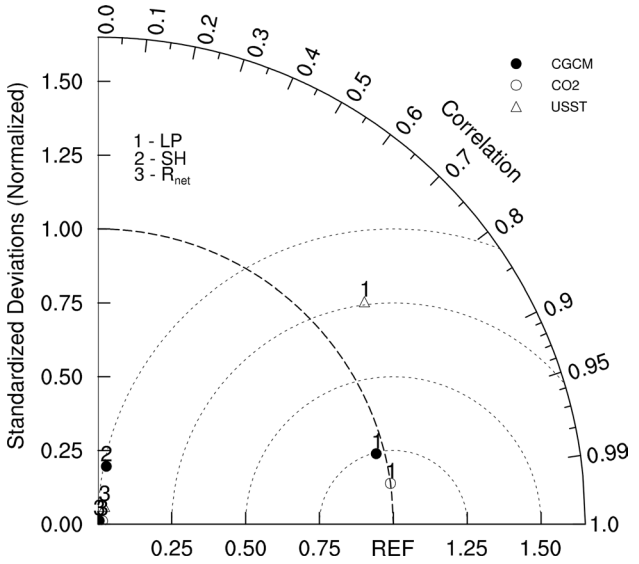

Fig. 3 Taylor diagram displaying the similarity of the LH, sensible heating at the surface and net radiation of the atmosphere to the JJAS HS response. The dots, circles and triangles are the results in the CGCM, CO2 and USST, respectively. Only the MME results are shown. The numbers 1, 2 and 3 denote the LH, surface sensible heating, and net radiation of the atmosphere, respectively. The ratio of the spatial standardized deviation and the spatial correlations are indicated by the radial distance and radial angle, respectively. The distance to "REF" is the center root-mean-square error. The results of surface sensible heating in the CO2 and USST are not displayed because the correlation coefficients are negative

Although the LH change in response to increased CO_2 is diagnosed in Qu et al. (2020), (1) the results are presented here to facilitate a better understanding of the effects of CO_2 direct radiation and uniform oceanic warming, and (2) the 11-model results are not strictly identical to that of the 30-model in Qu et al. (2020). Figure 4 illustrates the diagnostic results associated with Eq. (3). For the CGCM, the LH change is mainly a result of anomalous specific humidity transported by climatological ascending motion of the air (Fig. 4a, j). This term features significant enhancement over the TP. In response to increased CO_2, the TP surface warms. According to the Clausius–Clapeyron equation, the saturated water vapor and the specific humidity tend to increase (Fig. 5d). The increase is larger at the surface and reinforces the vertical humidity gradient. Accompanied by the transportation of climatological ascending motion of the air, the LH released to the atmosphere increases (Fig. 4a). The climatological specific humidity transported by anomalous ascending motion of the air slightly counteracts the HS increase (Fig. 4m).

The surface LH slightly favors the enhancement of the TP-averaged LH. The surface LH increases by 7.3 W m^{-2} in the CGCM results. The surface LH exchange is linked to surface evaporation. Based on the formula for the LH over a surface (Du et al. 2009), the change in potential evaporation over land can be written as follows:

$$E' = E_1 + E_2 + E_3 + E_4 + E_5 \tag{4}$$

where

$$E_1 = \overline{\rho_a} C_E \overline{W} \left[q_s(\overline{T} + T') - q_s(\overline{T}) \right] \tag{5}$$

$$E_2 = \overline{\rho_a} C_E \overline{W} \left[-\overline{\mathrm{RH}} q_s(\overline{T_a} + T_a') + \overline{\mathrm{RH}} q_s(\overline{T_a}) \right] \tag{6}$$

$$E_3 = \overline{\rho_a} C_E \overline{W} \left[-\mathrm{RH}' q_s(\overline{T_a}) \right] \tag{7}$$

$$E_4 = \rho_a' C_E \overline{W} \left[q_s(\overline{T}) - \overline{\mathrm{RH}} q_s(\overline{T_a}) \right] \tag{8}$$

$$E_5 = \overline{\rho_a} C_E W' \left[q_s(\overline{T}) - \overline{\mathrm{RH}} q_s(\overline{T_a}) \right] \tag{9}$$

in which ρ_a is the surface air density, C_E is the transfer coefficient, W is the 10-m wind speed, q_s is the saturated specific humidity, T is the surface temperature, T_a is the air temperature at the surface, and RH is the relative humidity. The terms E_1, E_2, E_3, E_4 and E_5 represent the contributions of changes in the surface temperature, surface air temperature, relative humidity, air density and surface wind speed to the changes in potential evaporation, respectively. Figure 6 displays the TP-averaged terms of the JJAS potential evaporation divided by the transfer coefficient C_E. In the CGCM results, the enhanced potential evaporation over the TP mainly arises from the surface warming (Figs. 6 and 7a), which is a result of increased CO_2. This enhanced potential evaporation leads to the increase in surface LH released to the atmosphere. The finding is consistent with the results suggested by Laine et al. (2014).

In the CGCM results, the LH increase over the TP is mainly led by (1) moisture increases resulting from surface and atmosphere warming led by increased CO_2 and (2) evaporation intensification, which is also led by surface warming. Further investigation indicates that the above processes are led by CO_2 direct radiation and uniform sea surface warming.

4.1 CO_2 direct radiation

Consistent with the CGCM results, the moisture budget is diagnosed based on CO_2 results. Among the terms of Eq. (3), the LH change is mainly contributed by the mean specific humidity transported by anomalous vertical motion (Fig. 4n, 5b). This term features distinct enhancement over the southern TP. The CO_2 direct radiative effect

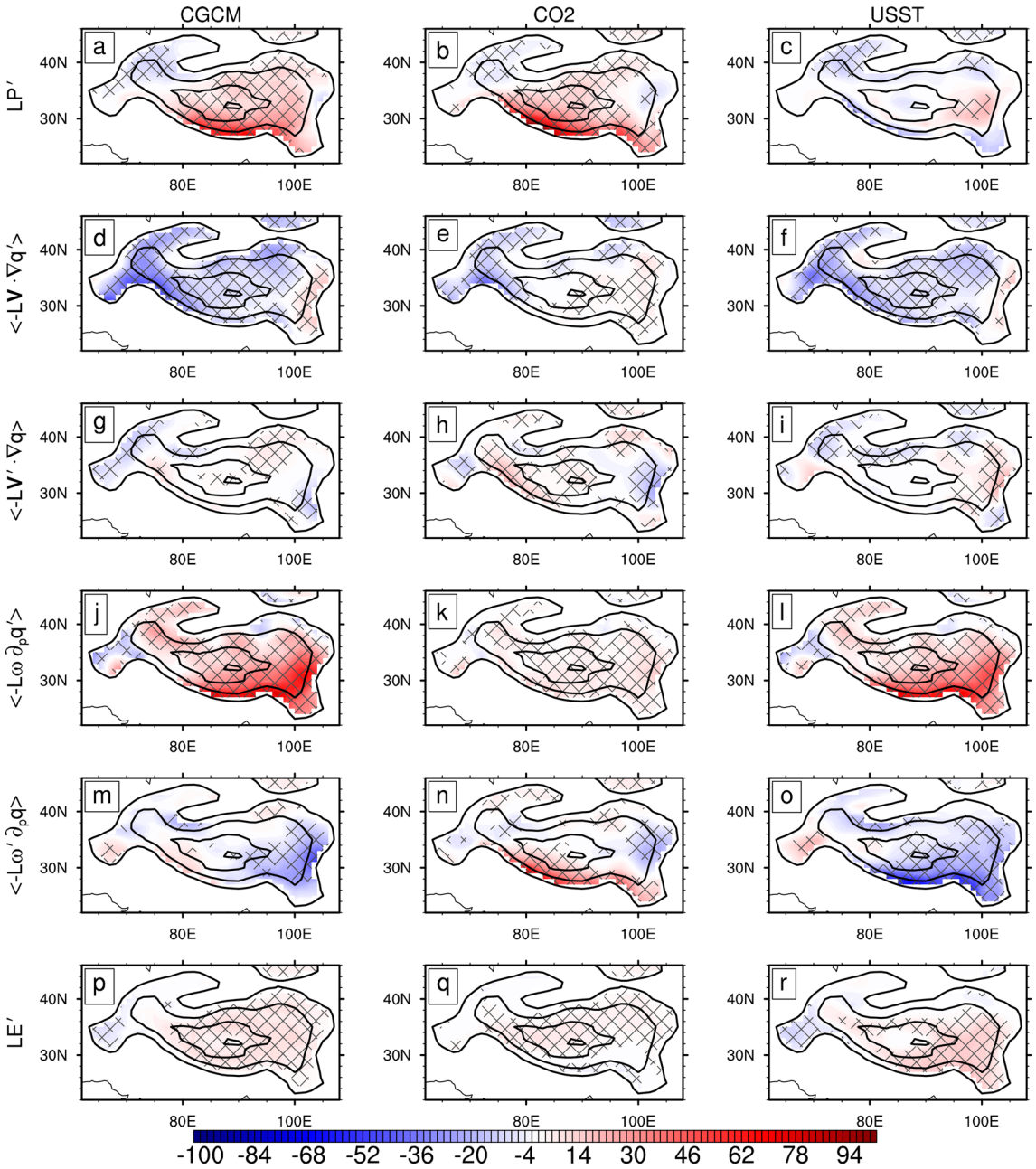

Fig. 4 JJAS-average of the LH and moisture budget terms of Eq (3) over the TP (color shading) for the CGCM (left column), CO2 (middle column) and USST (right column) results. The results have been multiplied by L and represent the mass integration from the surface to 100 hPa. Unit: W m^{-2}. The responses are the MME results. The contours represent elevations of 1500 m, 3000 m, 5000 m and 6000 m; and the lattices indicate that the response reached the 95% significance level

enlarges the land-sea thermal contrast (Kamae et al. 2014; Li and Ting 2017), resulting in enhanced ascending motion of the air over South Asia and southern TP (Fig. 5b). Because the change in near-surface specific humidity over the TP is slight (Fig. 5e), the anomalous specific humidity transported by mean vertical motion leads to a mild uniform rise over the TP (Fig. 4k). The anomalous specific humidity transported by the mean horizontal wind displays an overall decrease (Fig. 4e). The mean specific humidity transported by the anomalous horizontal wind is marginal (Fig. 4h). Compared with that of the mean specific humidity transported by anomalous vertical motion, the magnitudes of the last three terms are small. Thus, the change in ascending motion of the air is the key factor influencing CO_2 direct radiation on the LH over the TP.

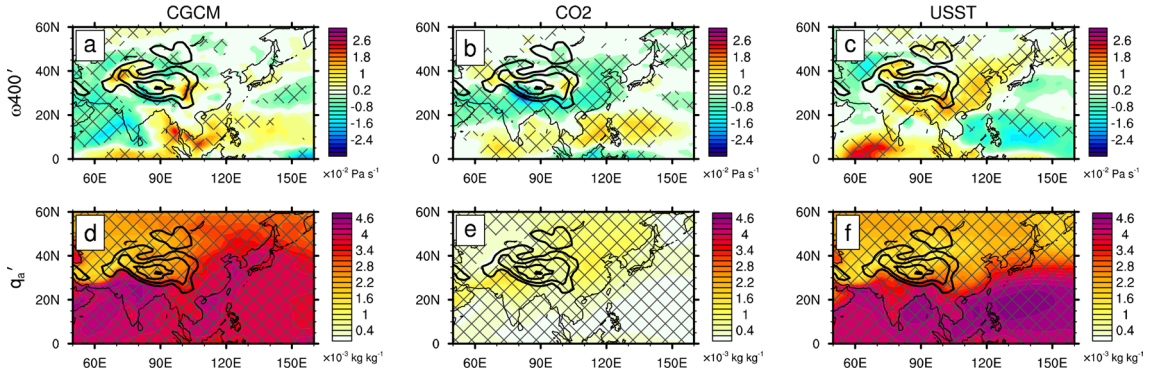

Fig. 5 JJAS-average responses (color shading) of ω at 400 hPa (1st row; unit: Pa s^{-1}), surface specific humidity (2nd row; unit: kg kg^{-1}) for the CGCM (left column), CO2 (middle column) and USST (right column) results. The responses are the MME results. The contours represent elevations of 1500 m, 3000 m, 5000 m and 6000 m; and the lattices indicate that the response reached the 95% significance level. bcc-csm1–1, MPI-ESM-LR and MPI-ESM-MR do not participate in the calculation because of the lack of surface specific humidity

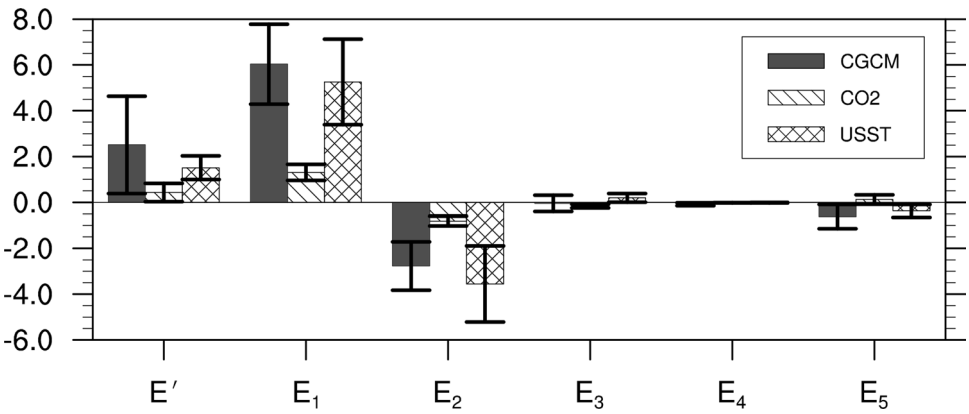

Fig. 6 TP-averaged terms [displayed in Eqs. (4)–(9)] of the JJAS potential evaporation for the CGCM (dark gray bars), CO2 (diagonal bars) and USST (lattice bars) results. Only those grid boxes at or above 3000 m over the TP were used to calculate the area average. The results have been divided by the transfer coefficient C_E. Unit: kg m^{-2} s^{-1}. The error bars represent the 95% CIs of the changes. The following models were not used in the calculation because of their lack of surface relative humidity or surface wind data: bcc-csm1–1, CCSM, MPI-ESM-LR, and MPI-ESM-MR

The surface LH slightly favors the enhancement of the TP-averaged LH. The surface LH increases by 3.3 W m^{-2} in the CO_2 results. The terms in Eqs. (4)–(9) are evaluated and displayed in Fig. 6. In the CO_2 results, the enhanced potential evaporation, as well as the actual evaporation, over the TP mainly arises from the surface warming (Figs. 6 and 7a). This surface warming is a result of CO_2 direct radiation.

In brief, the CO_2 direct radiation leads to (1) warming over the TP and South Asia, which yields an enlarged thermal contrast relative to the adjacent ocean and anomalous ascending motion of the air above the TP; and (2) warming in the TP surface, which results in enhanced evaporation. These factors lead to the strengthened LH released to the atmosphere.

4.2 Uniform sea surface warming

However, in the USST result, the LH change is generally insignificant over the TP (Figs. 2, 4c). To understand the LH change led by uniform sea surface warming, the associated moisture budget was diagnosed similarly. Among the terms of the moisture budget, the LH change is mainly the opposite-sign effects of the enhanced vertical gradient of specific humidity and weakened ascending motion of the air (Figs. 4l, o; 5c, f). The uniform increase in SST warms the atmosphere over the TP. According to the Clausius–Clapeyron equation, increased moisture is observed over the TP (Fig. 5f), with larger intensification near the surface, which yields an enhancement of the vertical gradient of specific humidity. The warming of the

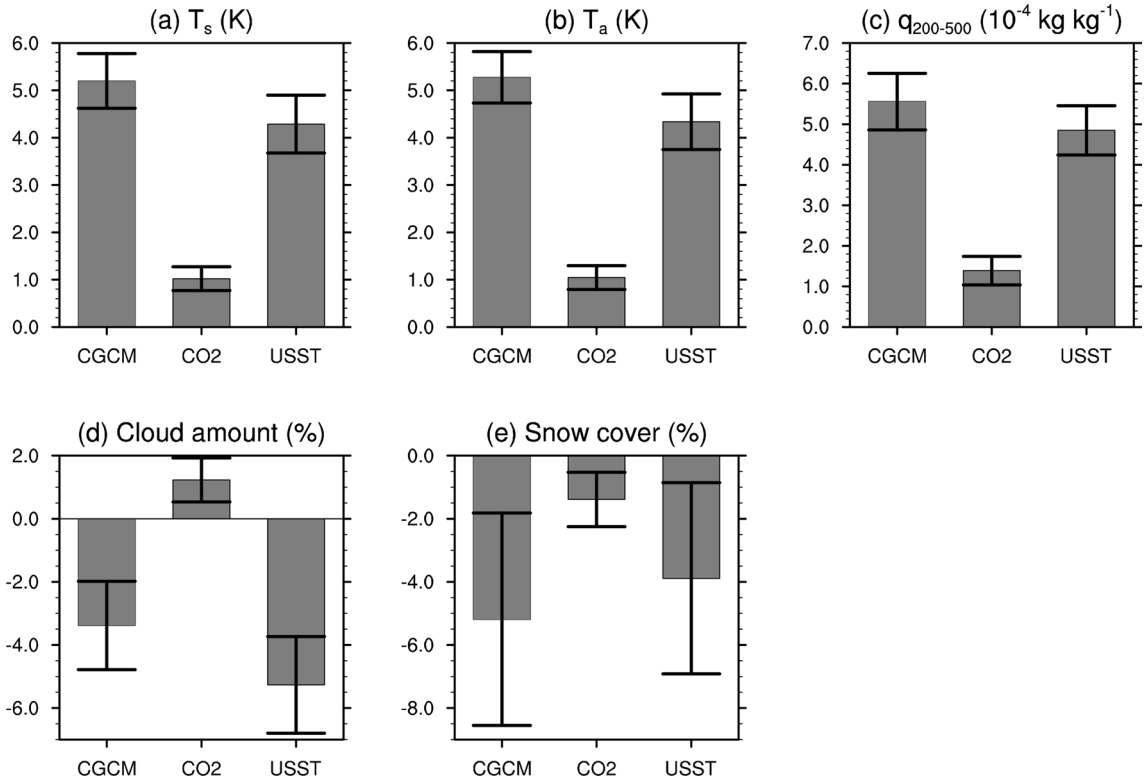

Fig. 7 TP-averaged responses of JJAS surface temperature (**a** unit: K), near-surface temperature (**b** unit: K), averaged moisture from 500 to 200 hPa (**e**, unit: 10^{-4} kg kg^{-1}), cloud amount (**c**, unit:%) and snow cover (**d**, unit: %) in the CGCM, CO2 and USST results. Only those grid boxes at or above 3000 m over the TP were used to calculate the area average. The error bars represent the 95% CIs of the changes. The following models did not participate in the calculation of snow cover because of lack of data: CCSM, HadGEM2-A(HadGEM2-ES), IPSL-CM5A-LR and IPSL-CM5B-LR

ocean narrows the land–ocean thermal contrast (Kamae et al. 2014), which may weaken the ascending motion of the air over the Asian monsoon region, including the TP (Fig. 5c). The competition of the two effects (increased atmospheric moisture and weakened ascending motion) results in the insignificant response of the LH.

The surface LH released to the atmosphere favors the LH increase. The surface LH increases by 4.6–7.4 W m^{-2} (95% CI) in the USST results. The potential evaporation over the TP is diagnosed based on Eqs. (4)–(9) and illustrated in Fig. 6. Similar to the finding in the CGCM and CO_2 results, the enhanced potential evaporation over the TP is mainly caused by surface warming (Figs. 6 and 7a). The amplitudes of the terms are larger in the USST results than the CO_2 results because the TP surface is heated to a greater degree under uniform sea surface warming than CO_2 direct radiation (Fig. 7a).

In the USST results, the LH increase over the TP is mainly led by (1) moisture increases resulting from surface and atmosphere warming led by uniform sea surface warming; and (2) evaporation intensification resulting from surface warming.

A comparison of the results of the CGCM, CO_2 and USST shows the following: (1) the HS increase in response to increased CO_2 is mainly the result of increased atmospheric moisture, which is mainly led by uniform sea surface warming; (2) uniform sea surface warming reduces the land-sea thermal contrast over East/South Asia and adjacent ocean and reduces the ascending motion of the air over the TP while CO_2 direct radiation enlarges the land–sea thermal contrast and the TP ascending motion; therefore, in the CGCM results, the contribution of the change in ascending motion of the air is slight; and (3) the HS increase over the TP is partly contributed by evaporation change, which is mainly led by surface warming resulting from uniform sea surface warming.

Because the response of surface sensible heating is weak and generally insignificant (Fig. 2), it is not discussed.

5 Net radiation

In the CGCM result, the net radiation of the atmosphere over the TP slightly increases and hinders the HS intensification (Fig. 2). This parameter represents the net effects of the

radiative responses at the surface and the TOA, and it is further led by the surface and atmosphere warming, increased atmospheric moisture, reduced cloud cover and shrinking snow cover (Fig. 7). This parameter is revealed in detail in Qu et al. (2020). This increase in net radiation is contributed by the combined effects of CO_2 direct radiation and uniform sea surface warming (Fig. 2). In the following, the contribution of the two effects to net radiation are investigated.

5.1 CO_2 direct radiation

The response of net radiation flux to CO_2 direct radiation favors the HS increase at the TP surface. Climatologically, the JJAS net radiation flux acts to cool the atmosphere, and it decreased by 3.1 W m^{-2} in the CO_2 results (Fig. 2), corresponding to a slight weakening of the cooling effect. The clear-sky results are analyzed by considering the effects of clouds on the radiation flux. The following clear-sky variables are available in the CMIP5 models: downwelling longwave radiation, downwelling shortwave radiation and upwelling shortwave radiation at the surface, and upwelling shortwave and longwave radiation at the TOA. The other radiation fluxes are treated the same as those in the all-sky results when we computed the clear-sky HS. The clear-sky net radiation decreases by 1.2 W m^{-2} (Fig. 8a). In the following, the associated radiation fluxes are investigated individually.

In the MME results, the downwelling longwave radiation at the surface increases by 9.3 W m^{-2} (Fig. 8a). A number of studies have estimated the downwelling longwave radiation at the surface (e.g., Cheng et al. 2013; Crawford and Duchon 1999; Duarte et al. 2006), and the quantitative assessment of this radiation flux is complicated. Roughly, it is determined by the near-surface temperature and cloud amount. The CO_2 direct radiative effect may lead to near-surface warming (Fig. 7b), which is beneficial to increasing longwave radiation. The 95% CI of the increase in all-sky downwelling longwave radiation is 7.0–11.7 W m^{-2} among the models, and that of the clear-sky results is 8.4–13.1 W m^{-2}. This finding suggested that the attendance of cloud-radiation feedback does not significantly affect the downwelling longwave radiation over the TP.

The upwelling longwave radiation at the TP surface increases by 5.2 W m^{-2} in the MME results (Fig. 8a). Following Stefan–Boltzmann's law, the radiation flux emitted from an idealized black body is as follows:

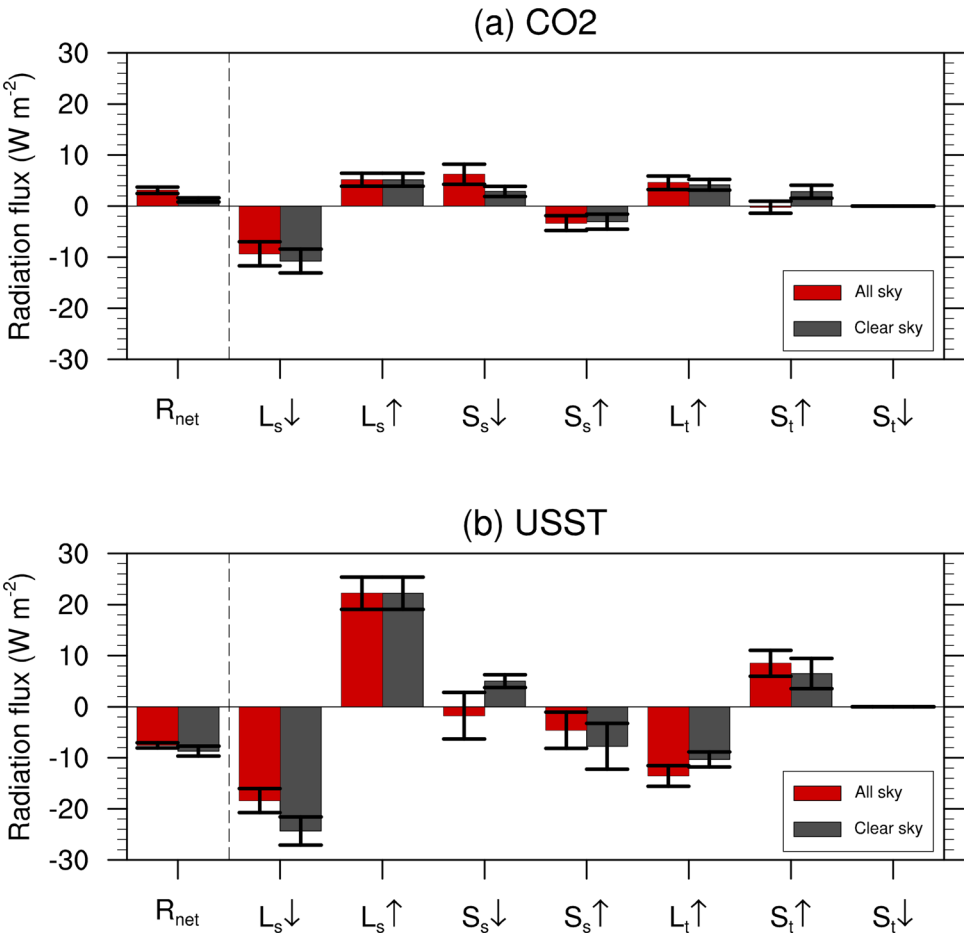

Fig. 8 JJAS-averaged responses of the net radiation of atmosphere, as well as the associated radiation fluxes. The bars in red and gray are the MME of all-sky and clear-sky results, respectively. Only those grid boxes at or above 3000 m over the TP were used to compute the average. The downwelling longwave and shortwave radiations and the upwelling longwave and shortwave radiations are multiplied by − 1. Therefore, positive and negative values indicate contributions of radiation gain and loss of the atmospheric column, respectively. Unit: W m^{-2}. The error bars represent the 95% CIs of the changes

$$B(T) = \delta T^4 \tag{10}$$

where $\delta = 5.67 \times 10^{-8}$ W m^{-2} K^{-4}. For the TP surface, δ may not be equal to this value. Supposing that the change in surface upwelling longwave radiation is solely contributed by temperature, then δ does not change and the relative change of upwelling longwave radiation flux at the surface may equal that of T^4. The 95% CI of the relative change of the increase in upwelling longwave radiation and T^4 over the TP are both (0.011, 0.018), indicating that surface warming (Fig. 7a) is able to explain the increase in upwelling longwave radiation flux at the TP surface.

The downwelling shortwave radiation at the TP surface declines by 6.2 W m^{-2} in the MME mean results (Fig. 8a), and atmospheric absorption under shortwave radiation and clouds is mainly responsible. The 95% CI of the decline in all-sky radiation is (4.3, 8.2) W m^{-2}; and that for the clear-sky result is (1.9, 3.9) W m^{-2}. Under the influence of CO_2 direct radiation, the water vapor increases due to environmental warming (Fig. 7b, c), and this increase causes intensified absorption of shortwave radiation and decreased downwelling shortwave radiation at the TP surface. Under cloud-radiation feedback, the increased cloud cover (Fig. 7d) further reduces the shortwave radiation reaching the surface. This increased cloud amount mainly results from the overall enhanced ascending motion of the air over the TP in response to CO_2 direct radiation (Fig. 5b).The MME-mean upwelling shortwave radiation at the TP surface decreases by 3.3 W m^{-2} (Fig. 8a). Under the influences of CO_2 direct radiation, the TP-averaged snow cover slightly reduces (95% CI 0.5%, 2.3%; Fig. 7e), leading to a mild reduction in albedo (95% CI 0.6%, 2.3%). If the downwelling shortwave radiation to the TP surface is held fixed, then the reduction in albedo contributes to a decline in upwelling shortwave radiation of 0.8–2.7 W m^{-2} (95% CI), whereas if the albedo is fixed, then the changes in downwelling shortwave radiation contribute to a decrease in upwelling shortwave radiation by 1.0–2.2 W m^{-2} (95% CI). These results reflect that the changes in downwelling shortwave radiation and albedo at the TP surface equally lead to decreases in upwelling shortwave radiation.

In the CO_2 results, the outgoing longwave radiation at the TOA over the TP decreases by 3.3–5.9 W m^{-2} (95% CI) among the models, with the MME at 4.6 W m^{-2} (Fig. 8a). The corresponding decrease of clear-sky results is 3.1–5.2 W m^{-2} (95% CI), indicating an insignificant effect of cloud-radiation feedback. The decreases are due to the higher concentration of CO_2, which intercepts the longwave radiation outgoing into space.

The changes in outgoing shortwave radiation at the TOA over the TP is insignificant (95% CI − 1.4, 1.0 W m^{-2}; Fig. 8a) because of the offsetting effects of upwelling shortwave radiation at the TP surface and cloud-radiation feedback. The clear-sky outgoing shortwave radiation at the TOA decreases by 1.6–4.0 W m^{-2} (95% CI), and it is mainly led by decreases in clear-sky upwelling shortwave radiation at the TP surface, which is 1.6–4.5 W m^{-2} (95% CI). Cloud-radiation feedback acts to increase the radiation possibly through (1) increasing the reflection of shortwave radiation by cloud; (2) reducing shortwave radiation reaching the TP surface and that absorbed by the surface; and (3) blocking the upwelling shortwave radiation from surface to the TOA.

Therefore, over the TP, CO_2 radiative effects lead to warming at the surface and above the atmosphere, increased atmospheric moisture, enhanced atmospheric absorption of longwave radiation, increased cloud cover and reduced snow cover. Consequently, the increased upwelling longwave radiation at the surface, decreased downwelling shortwave radiation at the surface and outgoing longwave radiation at the TOA favor the reduction of net radiation, whereas the increased downwelling longwave radiation and upwelling shortwave radiation at the surface intensify the net radiation. Finally, the net radiation declines.

5.2 Uniform sea surface warming

The response of net radiation flux to uniform sea surface warming slightly hinders the HS increase at the TP surface. The net radiation increases by 7.6 W m^{-2} (95% CI 7.1–8.1 W m^{-2}) in the USST results (Fig. 2), corresponding to a slight weakening of the cooling effect. The clear-sky net radiation increases by 8.7 W m^{-2} (95% CI 7.7–9.7 W m^{-2}), displaying an insignificant difference relative to the all-sky result (Fig. 8b). In the following, the relevant radiation fluxes are studied individually.

In the MME results, the downwelling longwave radiation at the surface increases by 16.1–20.7 W m^{-2} (95% CI; Fig. 8b), and the corresponding clear-sky result is 21.6–27.1 W m^{-2} (95% CI). Because the downwelling longwave radiation at the surface is determined by the near-surface temperature and cloud cover (e.g., Cheng et al. 2013; Crawford and Duchon 1999; Duarte et al. 2006), the clear-sky downwelling longwave radiation results indicate that near-surface warming (Fig. 7b) is the most important factor leading to the increase of downwelling longwave radiation. The difference between all-sky and clear sky results indicates that cloud-radiation feedback significantly but partly offsets the increases in downwelling longwave radiation at the TP surface.

The upwelling longwave radiation at the TP surface increases by 19.1–25.4 W m^{-2} (95% CI) among the models (Fig. 8b). The relative changes of the increase in upwelling longwave radiation and T^4 over the TP are both calculated, and the 95% CI of these two parameters are (0.054, 0.072) and (0.053, 0.072), respectively. These nearly identical results indicate that the TP surface warming (Fig. 7a) is able

to explain the increase in upwelling longwave radiation flux led by uniform sea surface warming.

The changes in downwelling shortwave radiation at the TP surface are insignificant (95% CI − 6.3, 2.8 W m^{-2}; Fig. 8b). To better understand the radiation change, the clear-sky results are computed (95% CI 3.8, 6.2 W m^{-2}). Compared with CO_2 direct radiation, uniform sea surface warming may lead to more intensified atmospheric warming and moisture above the TP (Fig. 7b, c). Consequently, a larger increase in atmosphere absorption of shortwave radiation and a stronger decrease in downwelling shortwave radiation occur at the TP surface. The inclusion of cloud-radiation feedback in the models shows that clouds diminish the shortwave radiation reaching the surface and the amplitude of the decrease in downwelling shortwave radiation, and it also shows that the cloud cover is reduced (Fig. 7d) under weakened ascending motion of the air (Fig. 5b), which increases the shortwave radiation arriving at the TP surface. The synthetic effects of the atmospheric absorption of shortwave radiation and cloud result in the insignificant behavior of downwelling shortwave radiation at the TP surface.

Among the models, the upwelling shortwave radiation at the TP surface decreases by 1.0–8.1 W m^{-2} (95% CI; Fig. 8b). In the USST results, the TP-averaged snow cover reduces (95% CI 0.9%, 6.9%; Fig. 7e), which decreases the surface albedo (95% CI 1.8%, 6.7%). If the downwelling shortwave radiation reaching the TP surface is fixed, then the albedo reduction contributes to a decline in upwelling shortwave radiation of 2.0–7.7 W m^{-2} (95% CI), whereas if the albedo is fixed, then the downwelling shortwave radiation contributes to a mild change in upwelling shortwave radiation (95% CI − 1.4–1.2 W m^{-2}). The results reflect that in the USST results, the snow cover reduction is mainly responsible for the decrease in upwelling shortwave radiation at the TP surface.

In the USST results, the outgoing longwave radiation at the TOA over the TP increases by 11.5–15.6 W m^{-2} (95% CI; Fig. 8b) and the corresponding clear-sky results increase by 8.9–11.8 W m^{-2} (95% CI). These findings indicate that the effect of cloud-radiation feedback is insignificant. The increased outgoing longwave radiation at the TOA is mainly the result of surface and atmosphere warming (Fig. 7a, b).

The outgoing shortwave radiation at the TOA over the TP declines significantly (95% CI 6.0, 11.0 W m^{-2}; Fig. 8b). In response of uniform sea surface warming, the reduction of cloud cover (Fig. 7d) promotes the amount of shortwave radiation reaching the surface and atmosphere below the cloud; concurrently, the decline in the TP-surface albedo and above atmospheric absorption of shortwave radiation traps more shortwave radiation below the cloud cover, resulting in less shortwave radiation transmitted back to space.

Therefore, over the TP, uniform sea surface warming leads to the warming of the surface and upper atmosphere, the increased atmospheric moisture, and the reduced cloud cover and snow cover. Consequently, the increased upwelling longwave radiation at the surface and the decreased upwelling shortwave radiation at the TOA favor the reduction of net radiation over the TP, whereas the increased downwelling longwave radiation at the surface and outgoing longwave radiation at the TOA and the decreased upwelling shortwave radiation at the surface intensify the net radiation. Finally, the net radiation increases.

6 Model spread

The model spread of the TP HS response during JJAS is also largely explained by the sum of CO_2 and USST. First, the intermodel EOF method is performed on the HS responses over the domain [22–46°N, 62–108°E] in the CGCM results. The grid boxes at or above 1500 m are participating in the EOF analysis. The leading mode accounts for 46.0% of the total intermodel variance. The correlation coefficient between the leading principle component and the TP-averaged HS response across the models is 0.82. Then, the HS values of CGCM, CO_2, USST, PAT, CO_2 + USST, CO_2 + PAT, USST + PAT and CO_2 + USST + PAT are regressed onto the normalized leading principle component. The results are displayed in Fig. 9. The leading intermodel spread features an overall positive/negative anomaly of the HS response over the TP in individual models relative to the MME (Fig. 9a). It is easy to observe that the sum of CO_2 and USST is able to reconstruct similar features to that leading intermodel spread (Fig. 9e), and that the leading spread is mainly contributed by the USST results (Fig. 9c). Next, the effect of uniform sea surface warming on the intermodel spread is discussed.

Figure 10 demonstrates the intermodel regression of associated variables in the CGCM and USST results onto the normalized 1st principle component based on the intermodel EOF of the HS responses over the domain [22–46°N, 62–108°E] in the CGCM results. In response to uniform sea surface warming, the overall positive/negative deviation of the HS change over the TP in the individual models to the MME is mainly contributed by the deviation of LH responses (Figs. 9c, 10b). To further understand the possible causes, the LH change is diagnosed following Eq. (3). The deviation of the response of ascending motion of the air to the MME in the USST results is mainly responsible for leading the intermodel spread of the HS response over the TP in the CGCM results (Fig. 10d, f). The corresponding regression results of the CGCM displays a similar pattern and amplitude (Fig. 10a–c), confirming that the uniform sea surface warming mainly leads to the intermodel spread of HS responses in the CGCM results.

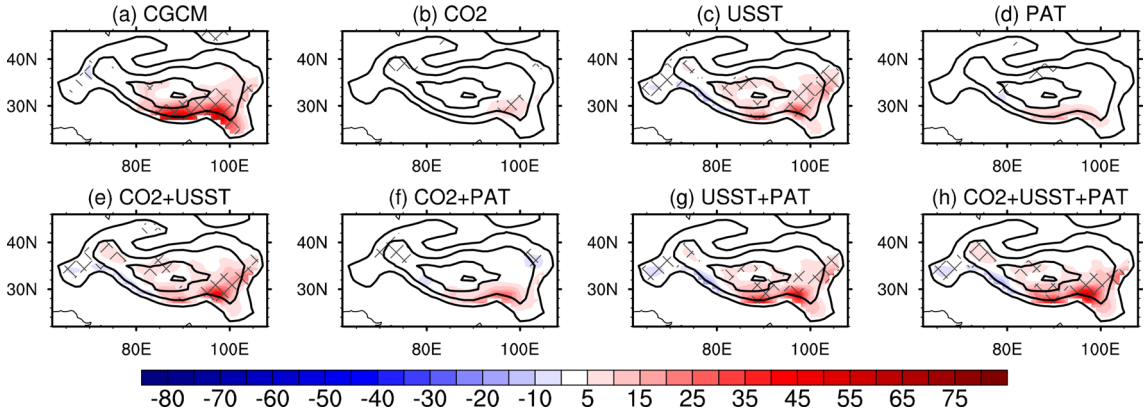

Fig. 9 Intermodel regression of the JJAS HS response (color shading) onto the normalized 1st principle component based on the intermodel EOF of HS responses over the domain [22–46 °N, 62–108 °E] in the CGCM results. The grid boxes at or above 1500 m are participating in the EOF analysis. The Tibetan Plateau (TP) is a huge **a**–**h** Results of CGCM, CO2, USST, PAT, CO2+USST, CO2+PAT, USST+PAT and CO2+USST+PAT. Unit: W m^{-2}. The contours represent elevations of 1500 m, 3000 m, 5000 m and 6000 m; and the lattices indicate that the regression reached the 90% significance level

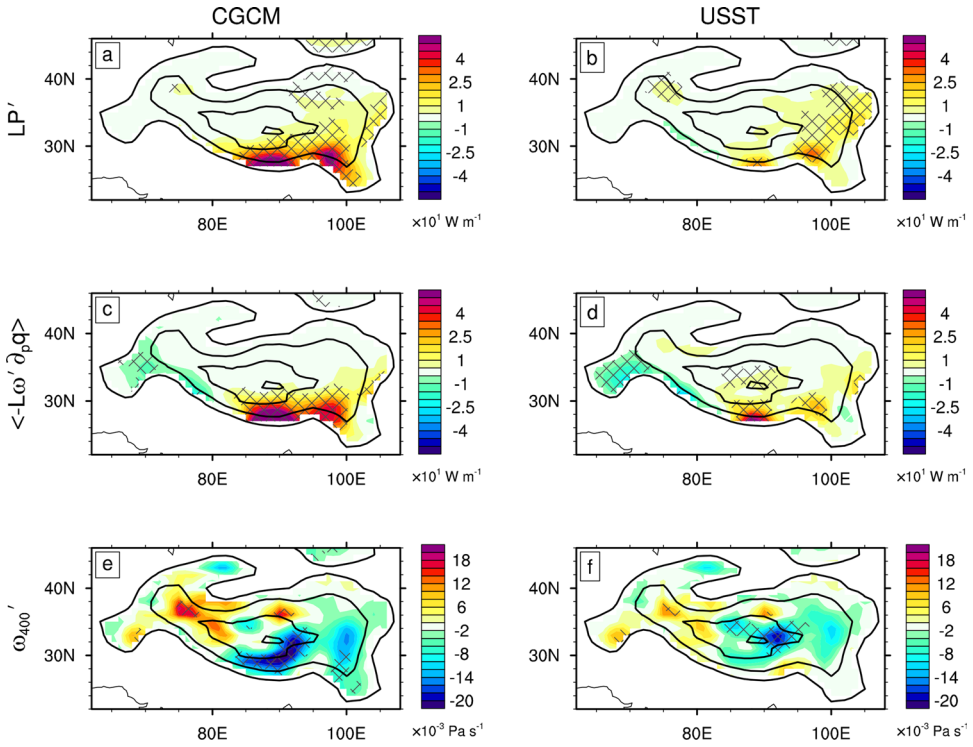

Fig. 10 Intermodel regression (color shading) onto the normalized 1st principle component, yielded by the intermodel EOF of HS responses over the domain [22–46 °N, 62–108 °E] in the CGCM results. The grid boxes at or above 1500 m are participating in the EOF analysis. The 1st, 2nd and 3rd row are the JJAS LH responses (unit: W m^{-2}), the climatological specific humidity transported by anomalous ascending motion of the air (multiplied by L; unit: W m^{-2}) and the pressure velocity response at 400 hPa (unit: Pa s^{-1}), respectively. The left and right columns are the CGCM and USST results, respectively. The contours represent elevations of 1500 m, 3000 m, 5000 m and 6000 m; and the lattices indicate that the regression reached the 90% significance level

In the USST results, the intermodel spread of the overall response of ascending motion of the air over the TP may partly originate from the amplitudes of the uniform sea surface warming among the models (although the sea surface warming in amip4K experiment relative to amip is 4 K, the warming in each model is scaled to the global mean sea surface warming in the CGCM results as introduced in Sect. 2.2). Interestingly, the intermodel correlation coefficient between the global mean sea surface warming and the leading principle component derived in Sect. 3 is − 0.10, indicating that uniform sea surface warming may not solely affect the leading spread of HS response in the CGCM. Because the large-scale ascending motion of the air over the TP depends on the land-sea thermal contrast, the association of this contrast with the leading spread of HS response is investigated. The average temperature between 200 and 500 hPa is defined as $T_{200\text{-}500}$; and then the area average of $T_{200\text{-}500}$ over the domain [10°S–20°N, 60–110°E] subtracted by that over the domain [22–46°N, 62–108°E] is regarded as the land-sea thermal contrast between the Indian

Ocean and the TP (note that in the calculation of the area average of $T_{200\text{-}500}$ over the domain [22–46°N, 62–108°E], the grids at or above 3000 m are included). The intermodel correlation coefficient between the land-sea thermal contrast in the USST results and the leading principle component of the TP HS response in the CGCM results derived in Sect. 3 is 0.53, which reaches a 90% significance level; moreover, the intermodel correlation coefficient between the land-sea thermal contrast in the CGCM results and the leading principle component is 0.52, which is also at the 90% significance level. This finding indicates that the temperature response above the TP to per unit global mean sea surface warming is not the same among the models.

The results reveal that in response to the increased CO_2, uncertainties exist in the global mean SST change. Along with the uncertainty in the overall warming response over the TP to global SST change, larger diversity occurs in the local change in ascending motion of the air and the LH released to the atmosphere. Finally, the diverse LH responses among the models contributes to the intermodel spread of the TP HS.

7 Summary and discussion

Based on the 1% CO_2 experiment of CMIP5, previous study (Qu et al. 2020) found that in response to increased CO_2 in the atmosphere, HS over the TP tends to enhance during JJAS. The multi-model ensemble pattern and the TP average, as well as the intermodel spread, of the HS enhancement are largely explained by the LH. The net radiation out of the atmosphere slightly intensifies and dampens the HS enhancement. Sequentially, based on the 1% CO_2 and amip-associated experiments of CMIP5, present study found that the influences of increased CO_2 in the atmosphere to HS over the TP can largely be explained by the CO_2 direct radiation and uniform sea surface warming.

In response to increased CO_2, during JJAS, the TP is dominated by increased HS (Qu et al. 2020). Significant increases mainly occur over the southern and eastern TP. The CO_2 direct radiation contributes to a uniform enhancement of the HS over the TP. The uniform sea surface warming leads to a mild and uniform decline in the TP HS. The SST pattern may contribute to a slight decrease in the HS over the southern TP. The sum of CO_2 direct radiation and uniform sea surface warming well reproduce the HS response to increased CO_2.

LH change mainly accounts for the HS enhancement in response to increased CO_2. When the CO_2 concentration in the atmosphere increases, the resultant uniform sea surface warming induces atmosphere warming over the TP. According to the Clausius–Clapeyron equation, the saturated water vapor and the specific humidity increase (Chou et al. 2009; Held and Soden 2006). The moisture increase is larger in the lower level than the upper level. Accompanied by climatological ascending motion of the air over the TP, the LH enhances. Atmosphere warming and moisturize changes also occur under only CO_2 direct radiation, although they are quite weak. In addition, the uniform warming of the ocean narrows the land-sea thermal contrast over East/South Asia and adjacent ocean (Li and Ting 2017) and reduces the ascending motion of the air over the TP, which was offset by the effect of CO_2 direct radiation, enlarging the land-sea thermal contrast. This offset results in the generally mild contribution of the change in ascending motion to the increased CO_2-induced LH variation. Additionally, uniform sea surface warming rises the temperature of the TP surface, causes local evaporation intensification and partly contributes to the HS increase over the TP.

Over the TP, the leading intermodel spread of the JJAS HS response to increased CO_2 features an overall positive/negative deviation relative to the MME HS response. The spatial pattern of the deviation is similar to that of the HS response in the MME results. This spread stems from the uniform sea surface warming. In individual models, uncertainties exist in the sea surface warming. Overlapping the uncertainty of the temperature response over the TP to the sea surface warming, the diversity in local change in ascending motion of the air is large, which leads to uncertainty in the LH response and HS response among the models. CO_2 direct radiation contributes quite little to that spread.

In response to increased CO_2, the overall net radiation of the atmosphere over the TP increases, partly hindering the HS intensification during JJAS. This increase in net radiation is mainly caused by uniform sea surface warming. The uniform rise of SST warms the TP surface and upper atmosphere, resulting in the increases in atmospheric moisture and the shrinkage of snow cover, and the weakened ascending motion of the air decreases the cloud amount. Consequently, the increase in upwelling longwave radiation at the surface and the decrease in upwelling shortwave radiation at the TOA favor the reduction of net radiation and contributes to enhancement of the HS over the TP, whereas the increase in downwelling longwave radiation at the surface and outgoing longwave radiation at the TOA and the decrease in upwelling shortwave radiation at the surface intensify the net radiation. Finally, the uniform sea surface warming intensifies the net radiation.

The above processes indicate that uniform sea surface warming reproduces most of the changes in key parameters under increased CO_2. However, the individual effect of uniform sea surface warming cannot reproduce the responses of LH and HS to increased CO_2. Although CO_2 direct radiation yields similar LH and HS responses, it is unable to reproduce the moisture, ascending motion of the air and cloud responses to increased CO_2. Thus, to well reproduce the key

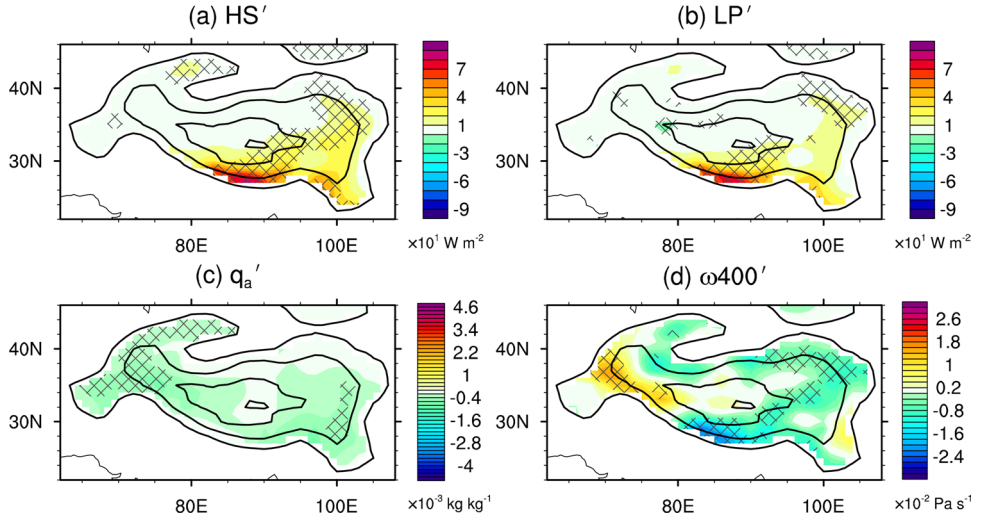

Fig. 11 JJAS mean responses (color shading) for the residual effect (CGCM minus the sum of CO_2, USST and PAT). **a–d** Results of the JJAS HS (unit: W m^{-2}), LH (unit: W m^{-2}), surface specific humidity (unit: kg kg^{-1}) and pressure velocity at 400 hPa (unit: Pa s^{-1}). The responses are the MME results. The contours represent the elevations of 1500 m, 3000 m, 5000 m and 6000 m; and the lattices indicate that the response reached the 95% significance level. bcc-csm1–1, MPI-ESM-LR and MPI-ESM-MR do not participate in the calculation for lack of surface specific humidity data. The label bars are set the same as those in Figs. 1 and 6 to facilitate comparison

features, neither the CO_2 direct radiation nor uniform sea surface warming should be excluded.

An unavoidable issue is the mismatch of the sum of CO_2 direct radiation, uniform sea surface warming and SST pattern with total effect. Since estimates of CO_2 direct radiation, uniform sea surface warming and SST pattern are based on the amip experiments, the residual effect mainly comes from the atmosphere–ocean interaction. The residual effect contributes significantly to the increase in JJAS HS over southern and northeastern TP (Fig. 11a). The HS response is mainly caused by LH change (Fig. 11b), which is further led by intensified ascending motion of the air (Fig. 11d). The moisture over the TP slightly reduces (Fig. 11c), leading to an opposite-sign contribution to HS increase. Compared with the combination of CO_2 and USST, the sum of CO_2, USST and residual effect better reproduces the increased CO_2-induced HS response. For the sum of CO_2 and USST, its spatial correlation coefficient with the HS response to increased CO_2 is 0.89, the ratio of its spatial standardized deviation with HS to that of the response to increased CO_2 is 0.91; and for the sum of CO_2, USST and residual effect, the results are 0.97 and 1.33. Because the key processes associated with HS response to increased CO_2 are well reproduced by the sum of CO_2 and USST and the residual effect does not contribute fundamentally to these processes, the residual effect is not further discussed.

Acknowledgement We acknowledge the World Climate Research Programme's Working Group on Coupled Modelling, which is responsible for CMIP, and we thank the climate modeling groups (listed in Table 1 of this paper) for producing and making available their model output. For CMIP the U.S. Department of Energy's Program for Climate Model Diagnosis and Intercomparison provides coordinating support and led development of software infrastructure in partnership with the Global Organization for Earth System Science Portals." The study was supported by the Strategic Priority Research Program of Chinese Academy of Sciences (XDA20060501), the National Natural Sciences Foundation of China (Grant No. 41831175), Key Deployment Project of Centre for Ocean Mega-Research of Science, Chinese Academy of Sciences (COMS2019Q03), the National Natural Sciences Foundation of China (Grant No. 41530425) and the Second Tibetan Plateau Scientific Expedition and Research (STEP) program (Grant No. 2019QZKK0102).

Appendix: Comparison of 11-model results with 30-model results

In the results of the 11 models, the JJAS HS is enhanced in response to increased CO_2, which is similar to the results of the 30 models (the model information is listed in Table S1 in the supplemental material). During JJAS, in the MME results of 11 models, the TP is dominated by a significantly increased HS. The largest increase mainly occurs over the southern TP, and the increased HS gradually weakens from south to north. The largest increase (~ 94 W m^{-2}) occurs over the southern TP in July (Fig. S1 in the supplemental material). The results of the 30 models display a similar response. However, the area reaching a 95% significance level is larger than that of the 11-model results, which may be due to the greater number of samples when calculating the significance.

The TP-averaged response of the HS and associated components do not display a significant difference between the

11- and 30-model results. In the MME of the 11-model results, the TP-averaged HS increases by 12.6 W m^{-2}, whereas in the MME of the 30-model results, the HS increases by 16.1 W m^{-2} (Fig. S2 in the supplemental material). However, the difference does not reach the 95% significance level. For the components of the HS, the differences are even smaller.

Consistent with the 30-model results, the LH is the main contributor to the HS pattern. Table S2 in the supplemental material demonstrates the spatial pattern correlation (of each variable with HS response) and the ratios of the spatial standardized deviation (of each variable to that of HS response). In the MME of 11-model results, the clear-sky HS is the closest to the HS (spatial correlation coefficient 1.00; ratios of the spatial standardized deviation 0.94), indicating that the cloud-radiation feedback is also negligible. In addition to the clear-sky HS, the LH is the closest among the components (spatial correlation coefficient 0.97; ratios of the spatial standardized deviation 0.97), revealing that the LH is the main contributor to the HS pattern. The spatial correlation coefficient and ratios of the spatial standardized deviation of sensible heating at the surface and net radiation flux into the atmosphere are much lower. These findings are similar to those in the 30-model results.

The intermodel spreads of the JJAS HS response over the TP in the 11- and 30-model results are compared. In both the 11- and 30 model results, the leading modes feature generally uniform diversity over the TP, with a maximum over the southern TP. The leading mode of the 11-model results accounts for 46% of the total intermodel variance, whereas that of the 30-model results accounts for 30.7% of the variance. When an intermodel regression of the variables is performed against the normalized leading principle components, the LH displays the most apparent results in both the 11- and 30-model results (Fig. S3 in the supplemental material), indicating that the LH contributes most to the leading intermodel spread of the HS over the TP in both cases. The second mode of the intermodel EOF features a seesaw structure over the central TP and the southeastern TP in both the 11- and 30-model results, which account for 20.3% and 22.9% of the variance, respectively. Consistent with the leading intermodel spread, the LH is also the most important contributor among the components (figures not shown). Thus, consistent with the 30-model results, the LH is mainly responsible for the intermodel spread in the 11-model results.

To summarize, in terms of the spatial pattern, the differences in the area average and intermodel spread of the HS over the TP between the 11-model and 30 model results are insignificant.

References

Abe M, Hori M, Yasunari T, Kitoh A (2013) Effects of the Tibetan Plateau on the onset of the summer monsoon in South Asia: The role of the air-sea interaction. J Geophys Res Atmos 118(4):1760–1776. https://doi.org/10.1002/jgrd.50210

Bony S, Bellon G, Klocke D, Sherwood S, Fermepin S, Denvil S (2013) Robust direct effect of carbon dioxide on tropical circulation and regional precipitation. Nat Geosci 6(6):447–451. https://doi.org/10.1038/ngeo1799

Boos WR, Kuang Z (2010) Dominant control of the South Asian monsoon by orographic insulation versus plateau heating. Nature 463(7278):218–222

Cheng J, Liang S, Yao Y, Zhang X (2013) Estimating the optimal broadband emissivity spectral range for calculating surface longwave net radiation. IEEE Geosci Remote Sens Lett 10(2):401–405. https://doi.org/10.1109/lgrs.2012.2206367

Chou C, Neelin JD, Chen CA, Tu JY (2009) Evaluating the "rich-get-richer" mechanism in tropical precipitation change under global warming. J Clim 22(8):1982–2005. https://doi.org/10.1175/2008JCLI2471.1

Crawford TM, Duchon CE (1999) An improved parameterization for estimating effective atmospheric emissivity for use in calculating daytime downwelling longwave radiation. J Appl Meteorol 38(4):474–480. https://doi.org/10.1175/1520-0450(1999)038<0474:Aipfee>2.0.Co;2

Du Y, Xie SP, Huang G, Hu K (2009) Role of air–sea interaction in the longpersistence of El Niño–induced North Indian Ocean warming. J Clim 22(8):2023–2038. https://doi.org/10.1175/2008JCLI2590.1

Duan AM, Wu GX (2008) Weakening trend in the atmospheric heat source over the tibetan plateau during recent decades. Part I Obser J Clim 21:3149–3164

Duarte HF, Dias NL, Maggiotto SR (2006) Assessing daytime downward longwave radiation estimates for clear and cloudy skies in Southern Brazil. Agric For Meteorol 139(3–4):171–181. https://doi.org/10.1016/j.agrformet.2006.06.008

Endo H, Kitoh A, Ueda H (2018) A unique feature of the Asian summer monsoon response to global warming: the role of different land–sea thermal contrast change between the lower and upper troposphere. SOLA 14:57–63. https://doi.org/10.2151/sola.2018-010

He J, Soden BJ (2015) Anthropogenic weakening of the tropical circulation: the relative roles of direct CO_2 forcing and sea surface temperature change. J Clim 28(22):8728–8742. https://doi.org/10.1175/JCLI-D-15-0205.1

He C, Wang Z, Zhou T, Li T (2019) Enhanced latent heating over the tibetan plateau as a key to the enhanced east asian summer monsoon circulation under a warming climate. J Clim 32(11):3373–3388. https://doi.org/10.1175/jcli-d-18-0427.1

Held IM, Soden BJ (2006) Robust responses of the hydrological cycle to global warming. J Clim 19(21):5686–5699. https://doi.org/10.1175/Jcli3990.1

Huang P, Xie S-P, Hu K, Huang G, Huang R (2013) Patterns of the seasonal response of tropical rainfall to global warming. Nat Geosci 6(5):357–361. https://doi.org/10.1038/ngeo1792

Kamae Y, Watanabe M, Kimoto M, Shiogama H (2014) Summertime land–sea thermal contrast and atmospheric circulation over East Asia in a warming climate—part II: importance of CO_2-induced continental warming. Clim Dyn 43(9–10):2569–2583

Kamae Y, Watanabe M, Ogura T, Yoshimori M, Shiogama H (2015) Rapid adjustments of cloud and hydrological cycle to increasing CO_2: a review. Curr Clim Change Rep 1(2):103–113. https://doi.org/10.1007/s40641-015-0007-5

Kamae Y, Ogura T, Watanabe M, Xie SP, Ueda H (2016) Robust cloud feedback over tropical land in a warming climate. J Geophys Res Atmos 121(6):2593–2609. https://doi.org/10.1002/2015jd024525

Kitoh A (2004) Effects of mountain uplift on East Asian summer climate investigated by a coupled atmosphere ocean GCM. J Clim 17(4):783–802. https://doi.org/10.1175/1520-0442(2004)017<0783:EOMUOE>2.0.CO;2

Laine A, Nakamura H, Nishii K, Miyasaka T (2014) A diagnostic study of future evaporation changes projected in CMIP5 climate models. Clim Dyn 42(9–10):2745–2761. https://doi.org/10.1007/s00382-014-2087-7

Lee JY, Wang B, Seo KH, Ha KJ, Kitoh A, Liu J (2015) Effects of mountain uplift on global monsoon precipitation. Asia Pacific J Atmos Sci 51(3):275–290. https://doi.org/10.1007/s13143-015-0077-2

Li X, Ting M (2017) Understanding the Asian summer monsoon response to greenhouse warming: the relative roles of direct radiative forcing and sea surface temperature change. Clim Dyn 49(7–8):2863–2880. https://doi.org/10.1007/s00382-016-3470-3

Li G, Xie SP (2014) Tropical biases in CMIP5 multimodel ensemble: the excessive equatorial pacific cold tongue and double ITCZ problems. J Clim 27(4):1765–1780. https://doi.org/10.1175/JCLI-D-13-00337.1

Li C, Yanai M (1996) The onset and interannual variability of the Asian summer monsoon in relation to land-sea thermal contrast. J Clim 9(2):358–375. https://doi.org/10.1175/1520-0442(1996)009<0358:TOAIVO>2.0.CO;2

Liu Y, Hoskins B, Blackburn M (2007) Impact of Tibetan orography and heating on the summer flow over Asia. J Meteor Soc Jpn 85:1–19. https://doi.org/10.2151/jmsj.85B.1

Luo H, Yanai M (1984) 1979 part II: heat and moisture budgets. Mon Wea Rev 112(5):966–989. https://doi.org/10.1175/1520-0493(1984)112<0966:TLSCAH>2.0.CO;2

Ma J, Xie SP (2013) Regional patterns of sea surface temperature change: a source of uncertainty in future projections of precipitation and atmospheric circulation. J Clim 26(8):2482–2501. https://doi.org/10.1175/JCLI-D-12-00283.1

Ma J, Xie SP, Kosaka Y (2012) Mechanisms for tropical tropospheric circulation change in response to global warming. J Clim 25(8):2979–2994. https://doi.org/10.1175/JCLI-D-11-00048.1

Qu X (2017) The intermodel diversity of east Asia's summer rainfall among CMIP5 models. J Clim 30(22):9287–9301

Qu X, Huang G, Zhu L (2019) The CO_2-induced sensible heat changes over the Tibetan Plateau from November to April. Clim Dyn 53(9–10):5623–5635. https://doi.org/10.1007/s00382-019-04887-x

Qu X, Huang G, Zhu L (2020) CO_2-induced heat source changes over the Tibetan Plateau in boreal summer-Part I: the total effects of increased CO_2. Clim Dyn. https://doi.org/10.1007/s00382-020-05353-9

Sampe T, Xie SP (2010) Large-scale dynamics of the meiyu-baiu rainband: environmental forcing by the westerly jet. J Clim 23(1):113–134. https://doi.org/10.1175/2009JCLI3128.1

Shaw TA, Voigt A (2015) Tug of war on summertime circulation between radiative forcing and sea surface warming. Nat Geosci 8(7):560–566. https://doi.org/10.1038/ngeo2449

Sherwood SC, Bony S, Boucher O, Bretherton C, Forster PM, Gregory JM, Stevens B (2015) Adjustments in the forcing-feedback framework for understanding climate change. Bull Am Meteor Soc 96(2):217–228. https://doi.org/10.1175/bams-d-13-00167.1

Song JH, Kang HS, Byun YH, Hong SY (2010) Effects of the Tibetan Plateau on the Asian summer monsoon: a numerical case study using a regional climate model. Int J Climatol 30(5):743–759. https://doi.org/10.1002/joc.1906

Stocker TF, Qin D, Plattner GK, Alexander LV, Allen SK, Bindoff NL, Bréon FM, Church JA, Cubasch U, Emori S (2013) Technical Summary. In: Stocker TF, Qin D, Plattner G-K et al. (eds) Climate Change 2013: the physical science basis. Contribution of Working Group I to the Fifth Assessment Report of the Intergovernmental Panel on Climate Change. Cambridge University Press, Cambridge, UK and New York, NY, USA., p 79

Taylor KE, Stouffer RJ, Meehl GA (2012) An overview of CMIP5 and the experiment design. Bull Am Meteor Soc 93(4):485–498. https://doi.org/10.1175/BAMS-D-11-00094.1

Wang B, Ding Q (2008) Global monsoon: Dominant mode of annual variation in the tropics. Dyn Atmos Oceans 44(3–4):165–183. https://doi.org/10.1016/j.dynatmoce.2007.05.002

Wu G, Liu Y, He B, Bao Q, Duan A, Jin FF (2012) Thermal controls on the Asian summer monsoon. Sci Rep 2:404. https://doi.org/10.1038/srep00404

Xie SP, Deser C, Vecchi GA, Ma J, Teng H, Wittenberg AT (2010) Global warming pattern formation: sea surface temperature and rainfall. J Clim 23(4):966–986. https://doi.org/10.1175/2009JCLI3329.1

Yeh DZ, Wu GX (1998) The role of the heat source of the Tibetan Plateau in the general circulation. Meteor Atmos Phys 67(1–4):181–198. https://doi.org/10.1007/bf01277509

Zhao Y, Duan AM, Wu GX, Sun RZ (2019) Response of the Indian Ocean to the Tibetan Plateau thermal forcing in late spring. J Clim 32(20):6917–6938. https://doi.org/10.1175/jcli-d-18-0880.1